A systematic search for lensed high-redshift galaxies in HST images of MACS clusters

A Repp, Harald Ebeling, J Richard

Monthly Notices
of the
ROYAL ASTRONOMICAL SOCIETY

MNRAS **457,** 1399–1409 (2016) doi:10.1093/mnras/stw002

A systematic search for lensed high-redshift galaxies in *HST* images of MACS clusters

A. Repp,[1]★ H. Ebeling[1] and J. Richard[2]

[1] *Institute for Astronomy, 2680 Woodlawn Dr., Honolulu, HI 96822, USA*
[2] *CRAL, Observatoire de Lyon, Université Lyon 1, 9 Avenue Ch. André, F-69561 Saint Genis Laval Cedex, France*

Accepted 2015 December 31. Received 2015 December 12; in original form 2015 June 26

ABSTRACT

We present the results of a 135-arcmin^2 search for high-redshift galaxies lensed by 29 clusters from the MAssive Cluster and extended MAssive Cluster Surveys. We use relatively shallow images obtained with the *Hubble Space Telescope* in four passbands, namely, *F*606*W*, *F*814*W*, *F*110*W*, and *F*140*W*. We identify 130 *F*814*W* dropouts as candidates for galaxies at $z \gtrsim 6$. In order to fit the available broad-band photometry to galaxy spectral energy distribution (SED) templates, we develop a prior for the level of dust extinction at various redshifts. We also investigate the systematic biases incurred by the use of SED-fit software. The fits we obtain yield an estimate of 20 Lyman-break galaxies with photometric redshifts from $z \sim 7$ to 9. In addition, our survey has identified over 100 candidates with a significant probability of being lower redshift ($z \sim 2$) interlopers. We conclude that even as few as four broad-band filters – when combined with fitting the SEDs – are capable of isolating promising objects. Such surveys thus allow one both to probe the bright end ($M_{1500} \lesssim -19$) of the high-redshift ultraviolet luminosity function and to identify candidate massive evolved galaxies at lower redshifts.

Key words: galaxies: high-redshift – galaxies: statistics.

1 INTRODUCTION

Reionization and galaxy formation are key events in cosmic history; the former depends upon, and the latter is responsible for, the characteristics of high-redshift galaxies. Therefore, the study of such galaxies is a major component of the ongoing intensive investigation into the early epochs of the Universe.

The most credible redshift determinations arise from spectroscopic analysis. Although the catalogue of spectroscopically confirmed high-redshift galaxies continues to expand (e.g. Richard et al. 2011; Vanzella et al. 2011; Bradač et al. 2012; Bradley et al. 2012; Ono et al. 2012; Finkelstein et al. 2013, Oesch et al. 2015; Zitrin et al. 2015), the time required to obtain spectra of faint objects limits the scope of spectroscopic surveys. Hence, the most fruitful method for expanding the catalogue of high-redshift galaxies is the dropout technique (Steidel, Pettini & Hamilton 1995; Steidel et al. 1996), which relies on multiple-passband photometry. Breaks in an object's spectrum – in particular, both the Lyman break (at rest frame 912 Å) and the 4000-Å break – can cause it to 'drop out' of passbands blueward of the break due to absorption of its radiation by neutral gas. Comparison of the observed and rest-frame wavelengths of the break immediately yields a crude (photometric) redshift estimate. One can subsequently improve this estimate by fitting galaxy template spectral energy distributions (SEDs) to the observed multiband photometry.

Multiple researchers have applied this technique to identify both intermediate-redshift (Steidel et al. 1999; Ellis et al. 2001; Giavalisco et al. 2004; Ouchi et al. 2004; Stark et al. 2009; Oesch et al. 2010) and high-redshift galaxies (Beckwith et al. 2006; Bouwens et al. 2006, 2010, 2011; Ellis et al. 2013; Lorenzoni et al. 2013; Oesch et al. 2013; Schenker et al. 2013). The widest of these surveys have covered up to 1.65 deg^2 (e.g. Bowler et al. 2014).

To push this technique to fainter magnitudes, other studies have combined it with the power of gravitational lensing (Ellis et al. 2001; Richard et al. 2006, 2008; Atek et al. 2014; Bradley et al. 2014; Zheng et al. 2014); it was thus that Coe et al. (2013) identified a galaxy with photometric redshift $z \sim 11$ (see also Pirzkal et al. 2015). Lensed surveys tend to cover a smaller solid angle than field surveys because of their dependence on high-mass foreground galaxy clusters. One of the most extensive such projects is the Cluster Lensing And Supernova survey with Hubble (CLASH; Postman et al. 2012), which imaged 25 clusters in 16 filters, with integration times in each filter ranging from 1975 to 4920 s. (See for instance Zitrin et al. 2013, Bouwens et al. 2014 and Bradley et al. 2014.) Most lensed surveys apply more time to smaller solid angles; for instance, the Hubble Frontier Fields[1] programme devotes 140 orbits

★ E-mail: repp@ifa.hawaii.edu

[1] http://www.stsci.edu/hst/campaigns/frontier-fields

Table 1. Exposure times.

	Integration times				Filters	Clusters
	*F*606*W*	*F*814*W*	*F*110*W*	*F*140*W*		
This work	1200 s	1440 s	706 s	706 s	4	29
CLASH[a]	1975 s	4103 s	2415 s	2342 s	16	25

Note. [a]CLASH integration times are averages from table 5 of Postman et al. (2012). Actual exposure times vary from cluster to cluster, depending on the quality of previous observations.

to each of six massive clusters. Still ongoing, this deep-imaging programme has already detected a substantial number of high-redshift galaxies (see Atek et al. 2014, 2015; Zheng et al. 2014; Ishigaki et al. 2015; McLeod et al. 2015).

Despite these successes, photometric redshifts always contain an element of uncertainty, given the possibility of low-redshift objects mimicking the colours of high-redshift galaxies (Mobasher et al. 2005; Schaerer et al. 2007; Schenker et al. 2012). These low-redshift interlopers may be red stars or galaxies with high equivalent-width emission lines (Atek et al. 2011). Thus in searching for high-redshift dropouts, it is important to analyse passbands blueward of the dropout band in order to detect the flux enhancement due to strong emission lines (like H α and [O III]) which would indicate a lower redshift.

To summarize, one can increase the yield of photometric redshift surveys by employment of larger sample sizes, by utilization of gravitational lensing from massive galaxy clusters, and by a judicious choice of passbands. The most massive clusters known to date at $z > 0.3$ are those identified by the MAssive Cluster Survey (MACS; Ebeling, Edge & Henry 2001; Ebeling et al. 2007, 2010; Mann & Ebeling 2012), which systematically catalogued the most X-ray luminous – and hence the most massive – galaxy clusters. In this work, we employ the lensing power of 29 such clusters not studied by CLASH, thus conducting one of the broadest lensed dropout searches to date. Table 1 compares this survey to CLASH; despite the longer integration times and the greater number of passbands in CLASH, the similarity in solid angle coverage bodes well for the identification high-redshift candidates by our survey.

Throughout this paper, we assume a standard concordance cosmology with $H_0 = 70$ km s^{-1} Mpc^{-1}, $\Omega_m = 0.3$, and $\Omega_\Lambda = 0.7$. We express all magnitudes in the AB system (Oke & Gunn 1983).

2 DATA

This survey analyses *Hubble Space Telescope* (*HST*) images of the 28 MACS clusters and one eMACS (extended MACS) cluster (Ebeling et al. 2013) listed in Table 2. This sample comprises all MACS clusters that were not part of CLASH and for which *HST* images exist in all of the following passbands: *F*606*W* and *F*814*W* on the Advanced Camera for Surveys (ACS); and *F*110*W* and *F*140*W* on the Wide Field Camera 3 (WFC3). All images were obtained through *HST* Snapshot programmes.[2] The exposure times (identical within each passband across all clusters) appear in Table 1.

The WFC3 field of view (4.65 arcmin^2), being smaller than that of the ACS, determines the 135-arcmin^2 solid angle of this survey.

Table 2. Clusters surveyed, with Milky Way hydrogen column density (in units of 10^{20} cm^{-2}) for estimating extinction.

Cluster	n_H	Cluster	n_H
eMACSJ1057.5+5759	0.56	MACSJ1354.6+7715	2.86
MACSJ0140.0−0555	2.85	MACSJ1621.4+3810	1.12
MACSJ0152.5−2852	1.51	MACSJ1652.3+5534	2.33
MACSJ0257.6−2209	2.18	MACSJ1731.6+2252	6.29
MACSJ0451.9+0006	7.23	MACSJ1738.1+6006	3.74
MACSJ0712.3+5931	5.43	MACSJ1752.0+4440	3.06
MACSJ0916.1−0023	3.25	MACSJ2050.7+0123	7.50
MACSJ0947.2+7623	2.22	MACSJ2051.1+0215	8.14
MACSJ1115.2+5320	0.90	MACSJ2135.2−0102	4.27
MACSJ1124.5+4351	2.04	SMACSJ0234.7−5831	3.64
MACSJ1133.2+5008	1.44	SMACSJ0549.3−6205	4.50
MACSJ1142.4+5831	1.77	SMACSJ0600.2−4353	6.24
MACSJ1226.8+2153C	1.87	SMACSJ2031.8−4036	3.91
MACSJ1236.9+6311	1.68	SMACSJ2131.1−4019	3.00
MACSJ1319.9+7003	1.47		

3 ANALYSIS

One result of the opportunistic nature of the Snapshot programme is that the four images of each cluster are taken at random times dictated by scheduling requirements. As a result the images of a given cluster are not, in general, aligned. In addition, the ACS plate scale is significantly smaller than that of WFC3. In order to facilitate comparison between images in different passbands, we redrizzled all images (using DRIZZLEPAC[3]) to the pixel scale and reference frame defined by the *F*140*W* image for the relevant cluster.

The presence of low-sensitivity regions ('blobs' – see Dressel 2014) can complicate the analysis of WFC3 images. These artefacts are the result of differential reflectivity of the Channel Select Mechanism Mirror. In several instances (discussed in Section 6) one of these blobs (or another defect) in the *F*110*W* image coincides with both a detection in the *F*140*W* channel and dropout behaviour in *F*814*W* and *F*606*W* (see for instance the third image of Fig. 6). In addition, ambient light had contaminated the majority of the *F*110*W* image for a few clusters. (see for instance the fourth row of Fig. 5). In both of these situations, only three passbands of usable data are available.

We then stacked the *F*140*W* and *F*110*W* images and ran SExtractor (Bertin & Arnouts 1996) in dual-image mode, using the stacked image for detection. We employed a 12-pixel rectangular annulus for background determination and thus obtained a catalogue of objects with isophotal magnitudes in each passband. Our initial catalogue of SExtractor results comprise 37 809 records, the flux errors of which we corrected for correlated noise according to the prescription of Casertano et al. (2000). Since the WFC3 images determine our segmentation, and since the WFC3 point-spread function (PSF) is significantly wider than that of the ACS, we do not perform any PSF-matching. We want to capture as much flux as possible from the ACS images in order to insure that the objects we consider are truly dropping out in the ACS bands. By retaining the tighter ACS PSF, we allow for more accurate detection of this dropout behaviour.

The next task is to discriminate between galaxies, stars, and artefacts. To do so, we consider both the objects' morphology and their colours; we describe the morphological criterion here and the spectral criterion in Section 4.2. As Fig. 1 shows, point sources (stars)

[2] GO-10491, GO-10875, GO-12166, GO-12884: PI H.Ebeling

[3] http://drizzlepac.stsci.edu

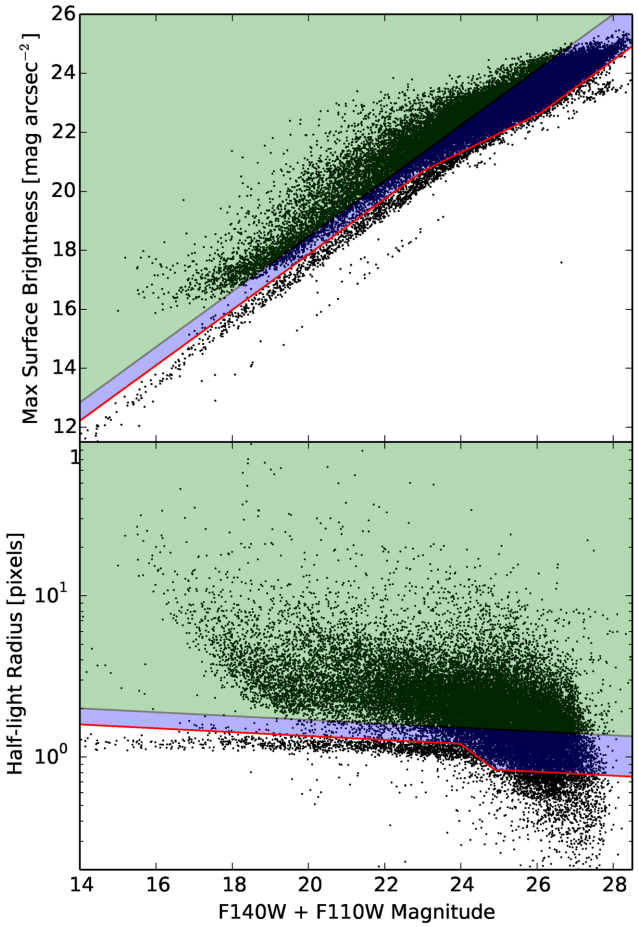

Figure 1. We use both morphology and SED to discriminate between stars and galaxies; these plots show our morphological criteria. In both panels the line corresponding to point sources (stars) is apparent, running diagonally in the top panel and (roughly) horizontally in the bottom panel. Any object below this line is more compact than a point source and thus must be an artefact. Hence we discard anything in the unshaded portion of either plot. Since the star line and the galaxy cloud begin to interpenetrate at higher magnitudes and since *HST* may not resolve compact faint high-redshift galaxies, we place this cutoff 1σ above the star line at low magnitudes and 2σ below the star line at high magnitudes. Any object in the light green (upper) region of both plots (3σ above the star line) we accept as a galaxy without further examination. The remaining objects (in the middle, blue-shaded region) we subject to the spectral criterion outlined in Section 4.2.

occupy a well-defined region (star line) in both magnitude/surface brightness space and magnitude/half-light radius space. Any object which lies more than 3σ above this line in both plots (i.e. in the light green regions of both panels of Fig. 1) we accept as a galaxy without further examination.

Ideally, we could now reject anything on this line as a star and anything below this line as an artefact. However, at higher magnitudes the galaxies begin to bleed into the star line; in addition, high-redshift galaxies can remain unresolved by WFC3 (Oesch et al. 2010). To account for these facts, we place the rejection limit 1σ above the star line at low magnitudes but 2σ below the star line at high magnitudes; anything that lies below this limit in either plot (i.e. in the unshaded region of either panel of Fig. 1) we reject as being either a star or an artefact.

The remaining objects lie in the blue region of the figure; we provisionally admit these objects into the next phase of our analysis but will use the spectral criterion of Section 4.2 to eliminate M-stars and brown dwarfs.

At this point, we also exclude detections in the noisy portions of the WFC3 field of view.[4]

We identify $F814W$ dropouts by requiring at least a 5σ detection in either WFC3 band ($F140W$ or $F110W$) and less than 2σ signal-to-noise ratio in both ACS bands ($F814W$ and $F606W$). We visually inspected the dropouts, eliminating diffraction spikes and areas in which a nearby bright source had corrupted the SExtractor results; we also eliminated 'detections' that appeared to be serendipitously grouped noise.

In addition, we checked the SExtractor segmentation map for these sources to ensure that SExtractor properly discriminated between the objects themselves and neighbouring sources. For cases in which it did not, we set an appropriate aperture for each object and reperformed the photometry in those apertures. In some cases, the aperture photometry resulted in at least a 2σ detection in the dropout band, causing us to eliminate these sources from consideration. Our final I_{814}-dropout catalogue consists of 130 sources.

Finally, to account for foreground (Milky Way) extinction, we first convert the column densities $n_{\rm H}$ from Table 2 to values of A_V using the prescription of Güver & Özel (2009) and then apply the Cardelli, Clayton & Mathis (1989) law to calculate the extinction in each band.

4 SED FITTING

4.1 Obtaining redshift probability distributions

Both the Lyman break and the 4000-Å break can cause dropout behaviour. Thus, a decrease in $F814W$ flux accompanied by a strong detection in $F110W$ could reflect the 4000-Å break redshifted to $1.5 \lesssim z \lesssim 2$ or the Lyman break redshifted to $7 \lesssim z \lesssim 10$. The lower redshift objects are likely to be massive, passively evolving galaxies. These galaxies (at such redshifts) typically are quiescent, extremely compact, and already quite old, with mass densities at least an order of magnitude greater than those of local elliptical galaxies (Toft et al. 2012, 2014). Some of these objects appear to be the cores about which the most massive of today's galaxies were built (van Dokkum et al. 2014). Since evolved $z \sim 2$ galaxies can serve as observational proxies for similar objects at higher redshifts, these interlopers are themselves promising candidates for future study.

However, our primary interest for this work is high-redshift galaxies; thus, to exclude low-redshift objects we fit galaxy template SEDs to the observed fluxes to obtain photometric redshifts for our candidates.

For this purpose we use BPZ[5] (Bayesian Photometric Redshift; Benítez 2000; Benítez et al. 2004; Coe et al. 2006), which matches an object's SED to known galactic spectral types and produces a probability distribution for the object's redshift.

However, BPZ's default templates do not allow one to include extinction as a separate parameter, although they do empirically

[4] We exclude detections within 15 pixels of the edge of the frame as well as in the defect near the bottom of the detector (dubbed the 'death star' in Dressel 2014), in addition to overexposed regions, defined as any region with a surface brightness of less than 15 magnitudes arcsec^{-2}.
[5] http://www.stsci.edu/dcoe/BPZ/

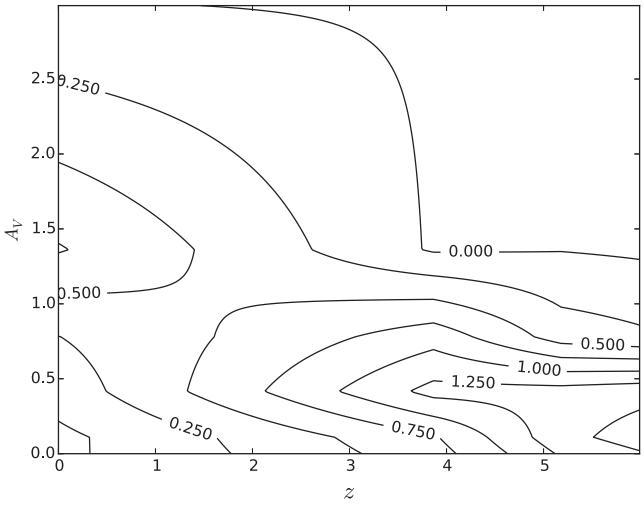

Figure 2. Contours showing prior probability distribution for intrinsic extinction A_V at a given redshift z, derived from data in Bouwens et al. (2009) and Magdis et al. (2010).

reproduce the observed photometry of the wide variety of galaxies observed in large-scale surveys (see, for example, Rafelski et al. 2015). We deemed it advisable to explicitly include a prior for intrinsic extinction, given the incidence of galaxies with non-negligible dust attenuation (e.g. Dey et al. 1999; Boone et al. 2011). We thus obtain dust-extinguished templates by applying the Calzetti et al. (2000) extinction law to each default template in increments of $\Delta A_V = 0.5$ from $A_V = 0$ to 3. Not all extinction values occur with equal probability, however, and the probability of extinction evolves with redshift. We therefore require a Bayesian prior for the likelihood of a given extinction A_V at a given redshift. To obtain such a prior, we employ the data from fig. 6 of Bouwens et al. (2009), who use observed ultraviolet (UV) continuum slopes β for a sample of Lyman break galaxies to derive estimates of $E(B-V)$ for redshifts from 2.5 to 6. Bouwens et al. (2009) also estimate the effective selection volume at each redshift, allowing calculation of the percentage of galaxies with a given intrinsic extinction (as a function of redshift). We extend these probabilities to the local Universe using the Magdis et al. (2010) estimate that galaxies are 8 to 10 times less obscured at $z \sim 2$ than they are now; and we extend them to higher redshifts by assuming the same probabilities obtained at $z \sim 6$. We then interpolate, smooth, and normalize the resulting distribution to obtain the prior shown in Fig. 2. One can obtain an analytic estimate for this distribution (Repp and Ebeling, in preparation), but for this work we simply employ the numerical probabilities plotted in the figure.

In addition to the extinction prior, we also require some assumptions about the probability of observing various galactic spectral types at various redshifts. BPZ derives its default $P(z|T)$ prior from the *Hubble Ultra-Deep Field (HUDF)*; however, since our area is so much larger than that of the *HUDF*, and since it – by design – includes large-scale structure, one must adopt a broader prior that considers galaxies over a wider range of redshifts and masses than those encountered in the *HUDF*. In formulating an alternative to the default prior, we must balance the need to rule out inherently improbable results (such as observing an elliptical galaxy at $z = 8$) with our limited knowledge of galaxy evolution.

We first rule out high-redshift ellipticals. We construct a Schechter luminosity function for elliptical galaxies using the following parameters, derived by Nakamura et al. (2003) from the Sloan Digital Sky Survey (SDSS): $M^*(r^*) = -21.52$; $\alpha = -0.83$; and $\phi^* = 1.61 \times 10^{-3}$ Mpc^{-3}. We then take the BPZ elliptical galaxy template, redshift it, account for intergalactic attenuation (Madau 1995), and convolve it with the $F140W$ filter profile. Thus, we derive an apparent magnitude for each combination of absolute magnitude and redshift. By combining this information with our $F140W$ limiting magnitude and the elliptical galaxy luminosity function, we obtain a prior for observing elliptical galaxies which vanishes smoothly around $z = 3.5$.

This constraint on elliptical galaxy visibility follows directly from the weakness of their UV emission combined with their empirically determined maximum luminosities. In recognition of the fact that the luminosity functions evolve with cosmic time (e.g. Bouwens et al. 2011, 2012), we assume flat priors for the other galactic spectral types. In particular, we have modified BPZ so that for each redshift, it reports the goodness-of-fit probability for the *most likely* galaxy template only, rather than summing the probabilities over all templates. (See also the discussion in Section 5.1 concerning comparison of BPZ results with results from HYPERZ.) Thus we consider only how closely the observed SED fits a galaxy template at high redshift without taking into account the (unknown) likelihood of each template.

To validate the utility of this modification, we next determined which procedure (original or modified BPZ) best reproduces the results of CLASH using only our four passbands. Since CLASH utilizes 16 passbands for their photometric redshift determinations, their multiple bands in essence function as very low-resolution spectroscopy. Thus, reproducing their redshifts would enhance our confidence that our procedure yields reliable results.

We began with 47 high-redshift galaxies from tables 5 and 6 of Bradley et al. (2014). For each galaxy, Bradley et al. (2014) report the photometric redshift estimate along with the 95 per cent (2σ) confidence interval. We obtained the magnitudes of each galaxy in our four passbands from the CLASH source catalogue.[6] We then ran both the original implementation of BPZ and our modified version (using the aforementioned prior on elliptical galaxies in both cases) on these 47 objects using only the four passbands considered in this project. From the BPZ results, we determined the most likely redshifts and 68 per cent (1σ) confidence intervals. Since, we only use four passbands whereas CLASH uses 16, we expect their 2σ confidence intervals to be roughly comparable to our 1σ intervals. Our limited number of passbands means that, in many cases, 95 per cent confidence intervals derived from our work would be so broad as to be almost useless. Thus for our own results, we quote 68 per cent intervals and, as noted in Section 7, recommend spectroscopic follow-up for our most plausible candidates.

The results appear in Fig. 3. We see that both versions of BPZ, when operating on only four passbands, give highest likelihood redshifts roughly comparable to those obtained by CLASH. The original version of BPZ, as might be expected, produces a more symmetric scatter about the diagonal $z_{\rm 4bands} = z_{\rm CLASH}$; it also results in fewer 'catastrophic outliers'. However, the results of the modified version are more conservative in that they seldom produce redshifts significantly in excess of the CLASH results. The greatest excess redshift (compared with CLASH) is $\Delta z = 0.5$ for the modified version, as opposed to $\Delta z = 1.5$ for the original version.

In two other respects our approach is conservative: first, we apply our extinction prior to all spectral types of galaxies, thus assuming that dusty ellipticals are as likely as dusty starbursts or spirals. Secondly, we use the SDSS $z = 0$ luminosity function for

[6] https://archive.stsci.edu/prepds/clash/

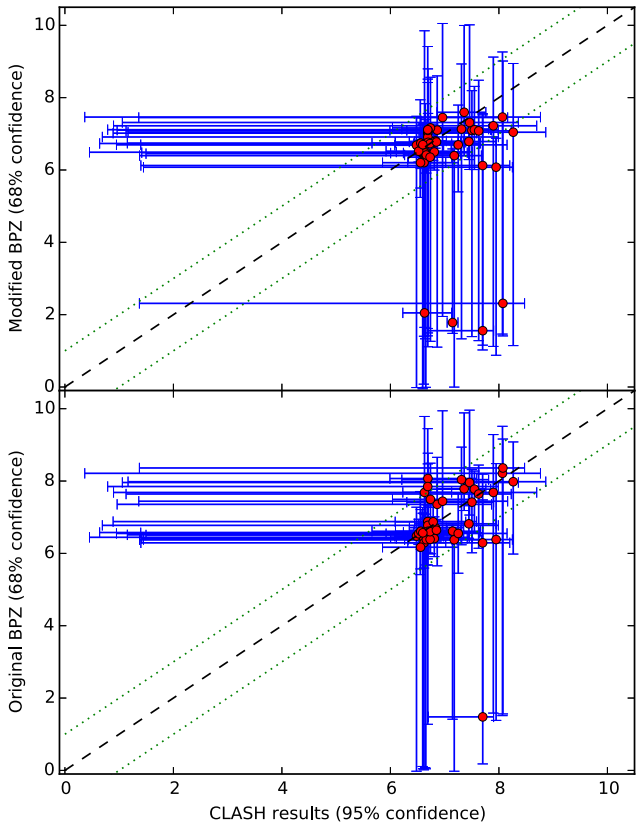

Figure 3. Comparison of photometric redshifts derived from CLASH with those derived from four passbands with BPZ (both the original version and as modified – see Section 4). Green dotted lines are $\Delta z = 1$ away from the main diagonal $z_{4\text{bands}} = z_{\text{CLASH}}$. The results of the original BPZ are more symmetric about the diagonal and have fewer catastrophic outliers. However, the modified version produces more conservative results, in that it is less likely to produce photometric redshifts significantly in excess of the (presumably more nearly correct) CLASH estimates.

ellipticals to estimate the likelihood of observing such galaxies at higher redshifts, thus neglecting evolution. As a result of these two assumptions, our estimated likelihood for dusty $z \sim 2$ ellipticals is probably higher than that found in the actual Universe. Given our limited number of passbands, our primary concern is to obtain conservative photometric redshifts; we are thus willing to accept results which might underestimate the true redshift. Hence, we use the modified version of BPZ, with the understanding that we probably underestimate to some degree the number of galaxies in each high-redshift bin.

4.2 Eliminating Stars and Substellar Objects

Section 3 outlines our two-fold approach to eliminating stars and substellar objects from our list of dropouts. The first aspect of our approach is the morphological criterion displayed in Fig. 1; any objects in the light green portions of this figure we accept as galaxies. However, objects in the blue portions of the figure have ambiguous morphology, and for these objects we use BPZ to determine how well their photometry matches what one would expect for M-stars and brown dwarfs.

To do so, we obtained composite spectra of M-, L-, and T-dwarfs by stacking 25 spectra (Burgasser et al. 2004, 2008, 2010; Burgasser, Burrows & Kirkpatrick 2006; Chiu et al. 2006; Burgasser 2007a,b; Kirkpatrick et al. 2010) of these objects obtained from the SpeX Prism Spectral Libraries.[7] We then included these spectra in the BPZ template list and, for these three spectral templates only, imposed a delta-function prior limiting them to $z = 0$.

We then prepared simulated stellar observations by convolving the model spectra with the *HST* filter profiles, scaling to magnitudes typical of our candidates and adding uncertainties typical of our candidates. Experimentation showed that, when applied to these simulated stars, BPZ with the extra templates yielded a probability spike at $z = 0$ that was typically at least 30 per cent of the maximum height of the distribution.

Thus, to impose our spectral criterion, we ran BPZ (with the extra templates) on each of our ambiguous candidates and eliminated those for which the probability density at $z = 0$ was at least 30 per cent of the maximum probability density. The remaining objects we retained as galaxies. Finally, we removed the stellar templates from BPZ's template library and reran it on these retained objects to obtain the probabilities reported in Table 5 and shown in Figs 5 and 6.

5 DISCUSSION

5.1 SED-fit Codes

There seems to be no 'standard' code for SED-fitting. Bradley et al. (2014) use BPZ, whereas Zheng et al. (2014) use a combination of BPZ and ISEDFIT. Atek et al. (2014) use HYPERZ; Bowler et al. (2014) use LEPHARE; and Oesch et al. (2013) use ZEBRA and EAZY. Others (McLure et al. 2011, 2013; Ellis et al. 2013) use proprietary code.

Since there is no accepted best SED-fit code (see Hildebrandt et al. 2010 for a review and evaluation of 17 photometric redshift codes), we thought it useful to compare the results of the two codes with which we are most familiar, namely BPZ (modified as described above) and HYPERZ[8] (Bolzonella, Miralles & Pelló 2000). BPZ marginalizes over a carefully selected set of galaxy templates (a feature which our modification largely circumvents) and naturally accommodates a prior distribution for those templates. It does not naturally handle various levels of intrinsic extinction, requiring us to handle extinction as described in Section 4. On the other hand, HYPERZ fits not only redshift but also extinction and metallicity; however, it does not seem to accommodate a prior on these variables.

Thus, we compare the results of two approaches: the first is a modified BPZ with an extinction prior and a limited galaxy template prior to disallow high-redshift ellipticals; the second is (unmodified) HYPERZ. The output appears in Fig. 4. We note first the high incidence of objects (blue points) to which the codes assign a probability distribution which is bimodal at a 68 per cent level (meaning that the 68 per cent confidence region is a topologically disconnected set). The majority of objects for which the 68 per cent BPZ and HYPERZ results differ (open circles) are these bimodal objects with poorly constrained redshifts. Secondly, as in the comparison with the CLASH results, we see that our modified version of BPZ is conservative in that it tends (with a few exceptions) to assign a *lower* redshift to (unimodal) objects than does HYPERZ. Thus, consistent with our conservative approach, we shall henceforth ignore all objects to which BPZ assigns a bimodal distribution at the 68 per cent level – i.e. we shall consider only the red points plotted in Fig. 4.

[7] http://pono.ucsd.edu/adam/browndwarfs/spexprism/library.html
[8] http://webast.ast.obs-mip.fr/hyperz/

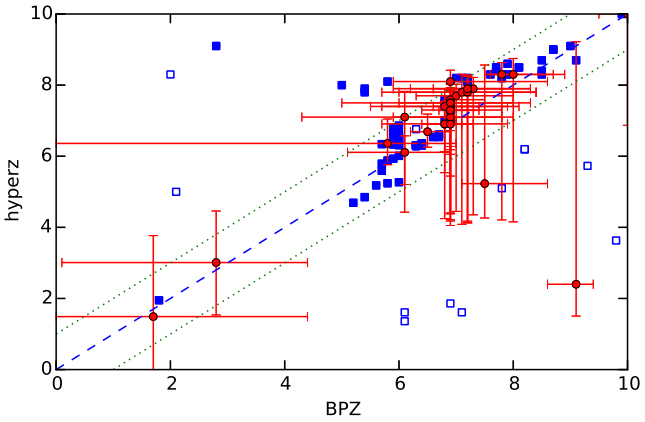

Figure 4. Photometric redshifts produced by BPZ (modified as described in Section 4) and by HYPERZ. Blue squares indicate probability distributions from BPZ which are bimodal at the 68 per cent level (i.e. the 68 per cent confidence regions are topologically disconnected), with only the most likely redshift plotted for each candidate. Red circles indicate unimodal distributions (connected 68 per cent confidence intervals). Filled markers indicate BPZ results which are consistent (to 68 per cent) with HYPERZ results; open markers indicate inconsistent results. Dotted lines show a distance of $\Delta z = 1$ from the main diagonal. For readability, we show error bars for consistent and unimodal distributions only. We use only the red data points (redshift probabilities unimodal at 68 per cent) for the remainder of our analysis.

Table 3. Magnifications obtained for high-redshift candidates.

Object ID[a]	Photo-z[b]	Amplification[c]	Nominal M_{1500}[d]
MACSJ0140−0851	$7.6^{+1.0}_{-0.2}$	1.26 ± 0.00	-22.8 ± 0.3
MACSJ0140−1028	$6.1^{+1.4}_{-1.5}$	7.04 ± 1.46	-18.4 ± 0.7
MACSJ0152−0651	$6.7^{+0.4}_{-0.4}$	10.03 ± 0.26	-18.6 ± 0.2
MACSJ0152−0871	$6.9^{+0.1}_{-0.1}$	7.25 ± 0.03	-21.9 ± 0.0
MACSJ0712−0608	$7.0^{+0.8}_{-0.8}$	1.24 ± 0.00	-21.1 ± 0.2
MACSJ0712−0699	$8.0^{+1.9}_{-0.5}$	1.51 ± 0.01	-23.1 ± 0.5
MACSJ0947−0072	$6.5^{+0.4}_{-0.3}$	1.17 ± 0.00	-22.2 ± 0.1
MACSJ1133−0922	$7.2^{+1.1}_{-1.0}$	1.28 ± 0.00	-21.3 ± 0.2
MACSJ2135−0509	$6.9^{+0.7}_{-0.4}$	5.15 ± 0.10	-19.7 ± 0.2
MACSJ2135−0763	$9.1^{+0.3}_{-0.5}$	1.41 ± 0.00	-23.8 ± 0.1

Notes. [a]See Table 5.
[b]68 per cent confidence intervals.
[c]Derived from LENSTOOL (Jullo & Kneib 2009) models.
[d]Uncertainties propagated from photo-z uncertainties.

5.2 Magnification

Determining the rest-frame UV magnitude of dropouts requires knowledge of the degree to which gravitational lensing has magnified the object in question. Determination of the lensing magnification requires in turn knowledge of the mass distribution of the foreground cluster.

Mass maps based on spectroscopy of strong-lensing features are available for a fraction of our target clusters, i.e. those for which such features have been spectroscopically confirmed. Magnification estimates were derived by means of LENSTOOL (Jullo & Kneib 2009) from the positions of strong-lensing features and a parametric model which includes the contribution from cluster-scale and galaxy-scale haloes (following the same approach as, e.g. Richard et al. 2010; Limousin et al. 2015). The available models allowed us to calculate the magnification due to cluster gravity for the 10 high-redshift candidates presented in Table 3. Note that the magnification errors include the statistical error from the parametric model but no systematic uncertainties from different modelling approaches. Although the uncertainties listed in Table 3 also include errors propagated from redshift uncertainties, they should thus be regarded as lower limits.

Some of these objects appear to be extremely luminous. Magnitudes below −22 are not unheard of;[9] however, Bouwens et al. (2011) note that UV magnitudes below −24 are physically unlikely, given that the vigorous star formation required for such luminosity would quickly fill the galaxy with dust. One of our objects (MACSJ2135−0763) approaches this limit of −24. One possible explanation is galaxy–galaxy lensing, given the nearby lower redshift galaxy visible immediately to the left (in the second row of Fig. 6). Another possibility is that the photometric redshift, despite being constrained by BPZ at the 68 per cent level, is in error. Inspection of its redshift probability distribution (Fig. 6) shows a non-negligible probability of $z \sim 2$; nevertheless, the probability of $z \geq 6.5$ is around 85 per cent (see Table 5). This object would merit additional investigation.

6 RESULTS

Given our extinction prior, our galaxy-type prior, and our modified version of BPZ, we determine both a posterior probability distribution and a best-fitting SED for each of the dropout galaxies. We retain only the 32 objects which meet the following criteria. First, the BPZ-derived probability distribution must peak at $z > 5.5$. Secondly, the probability distribution must be unimodal at the 68 per cent level; by this we mean that the 68 per cent confidence region (shaded blue in Figs 5 and 6) must be a connected set, so that only one peak rises to 68 per cent significance. Table 5 lists all 32 of these I_{814}-dropout galaxies, their magnitudes (corrected for Milky Way extinction) in each of the four passbands; their photometric redshifts; and their probabilities of falling into redshift bins $z \sim 7$, $z \sim 8$, and $z \sim 9$.

Note that two of these objects (eMACSJ1057−2279 and eMACSJ1057−2476 in Table 5) appear to be multiply lensed images of the same source. Both of these objects appear in the top row of Fig. 5; the first is in the centre of the stamp; the other is barely visible at the right-hand edge of the stamp. We make no attempt to determine the number of other objects in our sample which might be multiply lensed, and in this work we do not account for this source of systematic error in our sums of objects in each redshift bin.

The $F110W$ photometry of five of these objects is defective, as noted in Section 3. The objects appear at the end of Table 5; in addition, one of them appears in the third row of Fig. 5, and another appears in the third row of Fig. 6. For these objects, BPZ yields a relatively flat probability distribution at higher redshifts; in such cases, we weight the probability of galaxies' placement into redshift bins with the summed probabilities for the other dropout galaxies – in essence using the other galaxies' redshifts as a prior for those with defective $F110W$ photometry. Figs 5 and 6 show the images, probability distributions, and SEDs for some of the galaxies with the greatest likelihood of lying at a high redshift.

By summing the probabilities in Table 5, we obtain the total number of galaxies detected in each bin (also reported in Table 5),

[9] An example would be the object at $\alpha = 325.^{\circ}075\,3169$, $\delta = -23.^{\circ}677\,2512$ in table 4 of Bradley et al. (2014), which yields a rest-frame M_{1500} around −23, although the authors note a small possibility that the unresolved source might be a star.

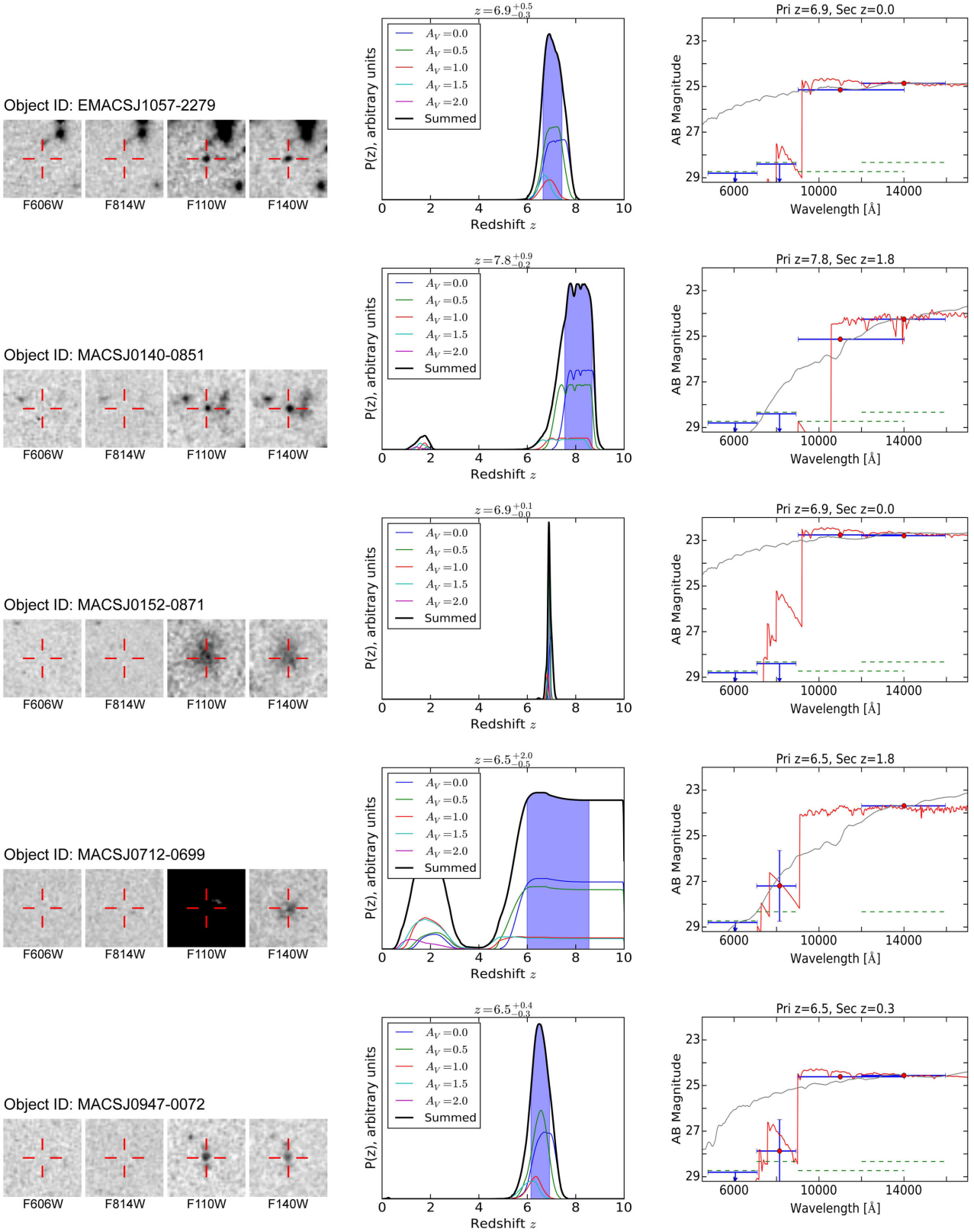

Figure 5. Images (5 arcsec per side), redshift probability distributions, and best-fitting SEDs for selected dropout galaxies. For object IDs see Table 5. Blue shading denotes 68 per cent confidence (also noted above the probability plots). Red SEDs show the most probable fit; grey SEDs show the most probable low-redshift fit. The best-fitting template for each case appears above the SED plot. Green dotted lines show limiting magnitude in each filter.

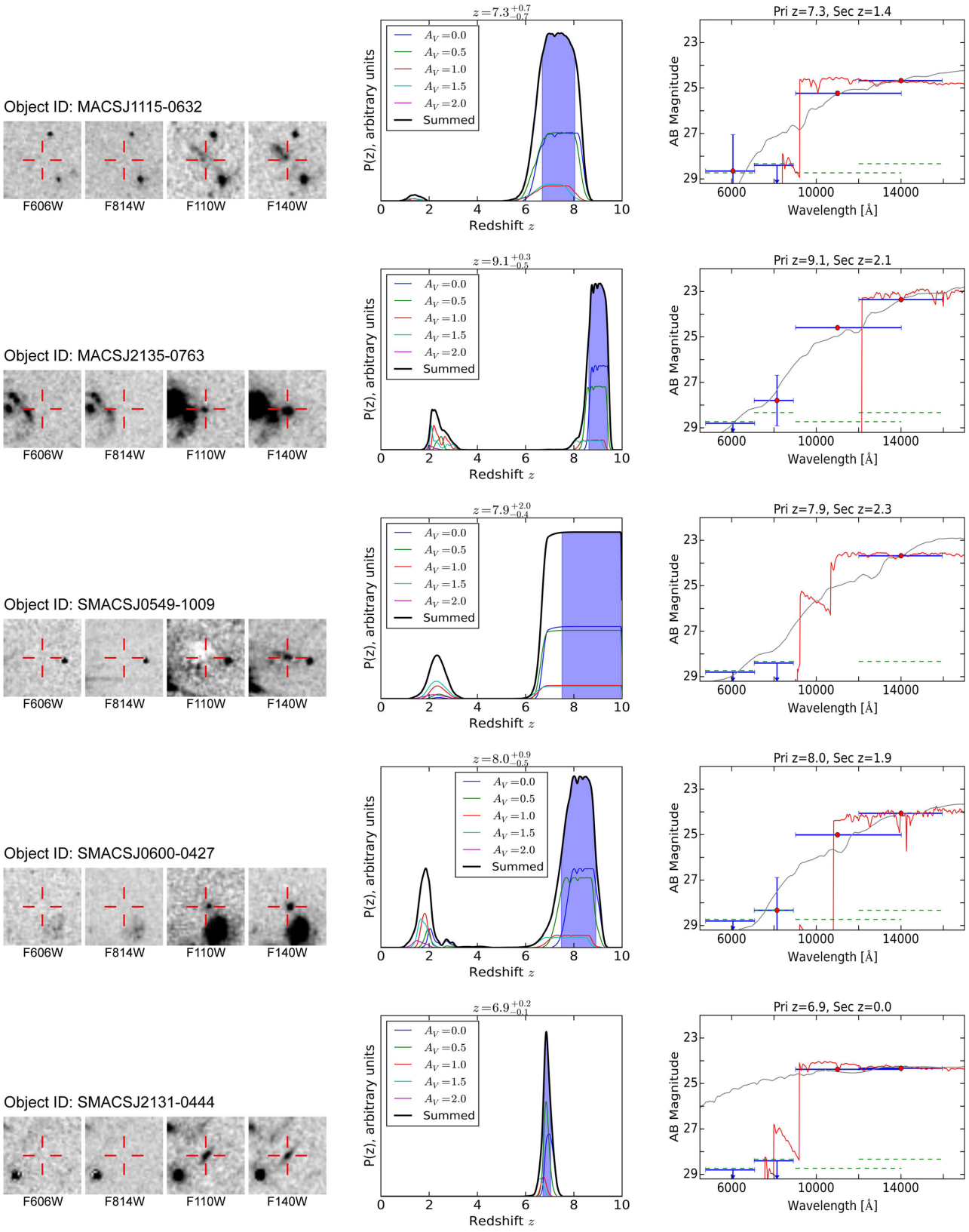

Figure 6. Images (5 arcsec per side), redshift probability distributions, and best-fitting SEDs for selected dropout galaxies. For object IDs see Table 5. Blue shading denotes 68 per cent confidence (also noted above the probability plots). Red SEDs show the most probable fit; grey SEDs show the most probable low-redshift fit. The best-fitting template for each case appears above the SED plot. Green dotted lines show limiting magnitude in each filter.

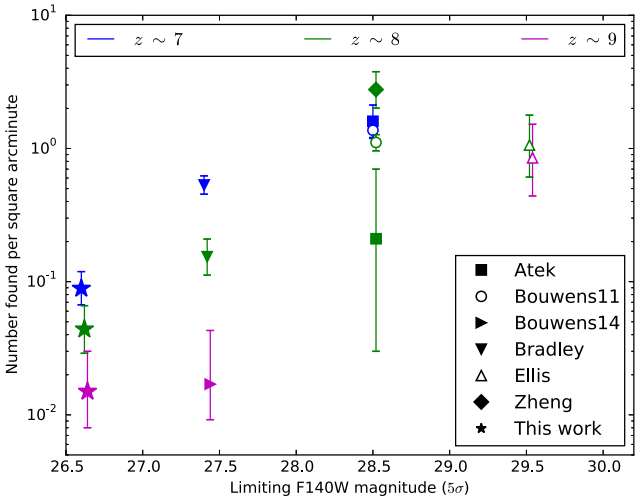

Figure 7. Comparison of the number of objects found in this work to that detected by other surveys, as a function of limiting magnitude. Filled symbols denote lensed surveys, and unfilled symbols denote unlensed surveys. (See Table 4 for details.) Blue markers indicate objects at $z \sim 7$; green at $z \sim 8$; and magenta at $z \sim 9$. Markers for $z \sim 8$ and $z \sim 9$ are slightly offset horizontally for clarity. Error bars represent Poisson confidence intervals. Note that for lensed surveys the vertical axis lists the number of objects per unit solid angle in the image plane, not the source plane.

Table 4. Surveys plotted in Fig. 7.

Reference	Survey/ Field(s)	Depth[a] (5σ)	Solid angle[b] (arcmin^2)
Atek et al. (2014)	Abell-2744 (HFF)	28.5	4.7
Bouwens et al. (2011)	HUDF09, ERS	28.5	53
Bouwens et al. (2014)	CLASH	27.4	77
Bradley et al. (2014)	CLASH	27.4	82
Ellis et al. (2013)	HUDF	29.5	4.7
Zheng et al. (2014)	Abell-2744 (HFF)	28.5	4.7
This work	MACS	26.6	135

Notes. [a]Limiting magnitude in *F*140*W* filter, or interpolated between *F*125*W* and *F*160*W* limiting magnitudes if *F*140*W* not utilized. If depths differ across fields in the same survey, we cite an average depth weighted by the solid angle of the fields involved.
[b]In image plane, not source plane.

which round to 12 galaxies at $z \sim 7$, 6 at $z \sim 8$, and 2 at $z \sim 9$. We thus estimate a total number of 20 high-redshift galaxies, which is one less than the sum of the above numbers due to rounding. (See the table for 68 per cent Poisson confidence intervals.)

Finally, in order to evaluate the effectiveness of our approach, we compare the number of high-redshift galaxies estimated in this survey with those detected by others. One would expect a positive correlation between the number of galaxies and the limiting magnitude of the survey. Using a thousand 0.4-arcsec-diameter apertures in each of our clusters, we determine that the 5σ limiting magnitude for our survey in *F*140*W* is 26.6. Normalizing the number of detected high-redshift objects to the solid angle coverage of various searches, and plotting the results against limiting magnitudes, we obtain Fig. 7. (See also Table 4 for the fields involved.)

Note that this figure combines surveys with disparate parameters (e.g. various detection bands, differing uniformity of depth, lensed/unlensed, etc.); thus one ought not to attempt to derive any sort of cumulative luminosity function from it. However, what Fig. 7 does show is that our survey returns a number of galaxies commensurate with our low limiting magnitude. It is the large solid angle of our survey that permits discovery of a non-negligible number of high-redshift candidates, underlining that shallow, wide surveys efficiently probe the bright end of the high-redshift UV luminosity function.

7 CONCLUSIONS

We draw the following conclusions from our survey. First, broad and relatively shallow surveys like ours can effectively detect high-redshift galaxy candidates. Devoting only about an hour of Hubble time to each of 29 clusters, we were able to identify 32 objects which have a probability distribution which peaks at high redshift and is unimodal at the 68 per cent level. Of these objects, we estimate that 20 lie at redshift $z \gtrsim 7$. Since our survey is relatively shallow, we are therefore sampling the bright end of the UV galaxy luminosity function at such redshifts. Our currently available mass maps suggest the existence of several extremely luminous objects with a photometric redshift of $z \sim 8$–9, placing them only about 600 Myr after decoupling. Such objects are ideal targets for further study, if for no other reason than to confirm or falsify the high photometric redshifts.

This further investigation is important for at least three reasons. First, despite our rejection of objects with significantly bimodal distributions, inspection of Table 5 shows that almost all of the remaining objects still have non-negligible lower redshift probabilities. Indeed, the summed likelihoods show that we can expect only 20 of the 32 listed objects to actually lie at $z \gtrsim 7$. Secondly, we derived our extinction prior from Lyman-break galaxy data, whereas low-redshift *F*814*W* dropouts represent a different population (4000-Å break galaxies and possibly some high-luminosity infrared galaxies). This population mismatch at lower redshifts could potentially introduce a systematic bias into our results. Thirdly, our analysis of BPZ and HYPERZ shows that the two codes can occasionally yield wildly divergent results. Thus, the choice of a specific SED-fit routine can introduce additional – and probably significant – systematic bias. We are unable to quantify these biases, and the resulting intrinsic uncertainty is not captured in the statistical error bars we report.

We note, however, that the low-redshift interlopers are scientifically interesting in their own right. Over 70 of our 124 *F*814*W*-dropout galaxies do not appear in Table 5 due to bimodalities in their probability distributions; thus, besides high-redshift candidates like those we report in this work, surveys such as ours can identify a large number of lower redshift objects conducive to the study of galaxy evolution.

Finally, we conclude that even as few as four broad-band filters suffice to isolate promising objects. However, our results also reinforce the importance of SED fitting in obtaining reliable photometric redshifts: dependence on a simple dropout criterion alone would have doubled our catalogue size by introducing objects with a significant likelihood of lying at low redshift. SED-fitting is especially important for surveys which utilize a small number of passbands; a greater number of passbands allows the use of more complex colour criteria (e.g. Castellano et al. 2010) which in practice function as a coarse SED fit. In particular, the *F*606*W* band was necessary to eliminate high equivalent-width emission-line galaxies from our sample. The small number of passbands did lead to a large number of objects with significantly bimodal photometric redshifts, which

Table 5. Dropout galaxies; all confidence intervals are 68 per cent.

ID	α_{J2000}	δ_{J2000}	m_{F606W}	m_{F814W}	m_{F110W}	m_{F140W}	z^a	$P_7{}^b$	$P_8{}^b$	$P_9{}^b$
Dropouts with reliable photometry in all four bands										
eMACSJ1057−2261	$10^h57^m32\overset{s}{.}02$	$57°59'30''$	>28.8	27.48 ± 0.69	26.04 ± 0.13	26.17 ± 0.20	$6.1^{+0.8}_{-1.0}$	0.19	0.01	0.00
eMACSJ1057−2279[c]	$10^h57^m27\overset{s}{.}80$	$57°59'7''$	>28.8	>28.4	25.15 ± 0.06	24.86 ± 0.06	$6.9^{+0.5}_{-0.3}$	0.79	0.14	0.00
eMACSJ1057−2476[c]	$10^h57^m27\overset{s}{.}48$	$57°59'7''$	>28.8	>28.4	24.55 ± 0.03	24.15 ± 0.03	$6.9^{+0.6}_{-0.1}$	0.74	0.25	0.00
MACSJ0140−0851	$1^h39^m58\overset{s}{.}63$	$-5°56'12''$	>28.8	>28.4	25.13 ± 0.05	24.25 ± 0.03	$7.8^{+0.9}_{-0.2}$	0.19	0.60	0.17
MACSJ0140−1028	$1^h40^m3\overset{s}{.}70$	$-5°55'15''$	>28.8	28.04 ± 0.97	26.38 ± 0.19	26.25 ± 0.24	$6.1^{+1.7}_{-1.8}$	0.19	0.09	0.01
MACSJ0152−0477	$1^h52^m33\overset{s}{.}16$	$-28°54'42''$	>28.8	>28.4	26.62 ± 0.16	26.35 ± 0.17	$6.9^{+1.2}_{-1.4}$	0.32	0.17	0.01
MACSJ0152−0651	$1^h52^m34\overset{s}{.}36$	$-28°54'27''$	>28.8	>28.4	25.89 ± 0.11	25.88 ± 0.16	$6.8^{+0.5}_{-0.4}$	0.67	0.07	0.00
MACSJ0152−0871	$1^h52^m36\overset{s}{.}05$	$-28°54'35''$	>28.8	>28.4	22.76 ± 0.02	22.79 ± 0.03	$6.9^{+0.1}_{-0.0}$	1.00	0.00	0.00
MACSJ0257−0913	$2^h57^m41\overset{s}{.}18$	$-22°10'10''$	>28.8	>28.4	26.23 ± 0.15	25.89 ± 0.14	$6.9^{+1.1}_{-0.9}$	0.37	0.23	0.01
MACSJ0712−0608	$7^h12^m13\overset{s}{.}17$	$59°32'52''$	>28.8	>28.4	25.99 ± 0.10	25.58 ± 0.10	$7.0^{+1.0}_{-0.7}$	0.43	0.25	0.00
MACSJ0947−0072	$9^h47^m17\overset{s}{.}86$	$76°24'21''$	>28.8	27.87 ± 1.37	24.62 ± 0.05	24.56 ± 0.07	$6.5^{+0.4}_{-0.3}$	0.53	0.00	0.00
MACSJ1115−0329	$11^h15^m15\overset{s}{.}94$	$53°19'5''$	28.28 ± 0.84	>28.4	26.35 ± 0.18	26.34 ± 0.25	$6.8^{+1.1}_{-1.1}$	0.39	0.13	0.01
MACSJ1115−0632	$11^h15^m17\overset{s}{.}45$	$53°20'27''$	28.65 ± 1.60	>28.4	25.23 ± 0.08	24.67 ± 0.07	$7.3^{+0.7}_{-0.7}$	0.48	0.39	0.01
MACSJ1124−0811	$11^h24^m28\overset{s}{.}77$	$43°50'41''$	>28.8	>28.4	26.38 ± 0.17	25.89 ± 0.15	$7.1^{+1.3}_{-1.4}$	0.28	0.25	0.04
MACSJ1133−0922	$11^h33^m8\overset{s}{.}33$	$50°8'27''$	28.63 ± 1.39	>28.4	25.98 ± 0.13	25.47 ± 0.12	$7.2^{+1.1}_{-1.0}$	0.35	0.29	0.02
MACSJ1621−0860	$16^h21^m23\overset{s}{.}01$	$38°11'13''$	>28.8	>28.4	26.51 ± 0.13	26.22 ± 0.14	$6.8^{+1.1}_{-1.1}$	0.36	0.17	0.00
MACSJ1652−0135	$16^h52^m26\overset{s}{.}52$	$55°34'43''$	>28.8	>28.4	26.81 ± 0.19	26.52 ± 0.20	$6.9^{+1.4}_{-1.9}$	0.26	0.17	0.02
MACSJ2051−0806	$20^h51^m13\overset{s}{.}80$	$2°16'48''$	>28.8	>28.4	26.32 ± 0.16	26.11 ± 0.18	$6.9^{+1.1}_{-1.0}$	0.39	0.18	0.01
MACSJ2135−0509	$21^h35^m10\overset{s}{.}90$	$-1°3'12''$	>28.8	>28.4	25.76 ± 0.14	25.52 ± 0.16	$6.9^{+0.9}_{-0.5}$	0.53	0.23	0.00
MACSJ2135−0763	$21^h35^m8\overset{s}{.}24$	$-1°2'41''$	>28.8	27.80 ± 1.11	24.59 ± 0.04	23.36 ± 0.02	$9.1^{+0.3}_{-0.5}$	0.00	0.07	0.78
MACSJ2135−1078	$21^h35^m14\overset{s}{.}82$	$-1°2'25''$	28.72 ± 2.05	>28.4	26.15 ± 0.18	25.69 ± 0.16	$7.2^{+1.2}_{-1.2}$	0.31	0.26	0.05
SMACSJ0600−0180	$6^h0^m9\overset{s}{.}21$	$-43°53'6''$	>28.8	28.04 ± 1.19	25.48 ± 0.11	24.81 ± 0.08	$6.9^{+1.7}_{-1.0}$	0.27	0.26	0.03
SMACSJ0600−0427	$6^h0^m9\overset{s}{.}12$	$-43°53'44''$	>28.8	28.33 ± 1.44	25.01 ± 0.07	24.06 ± 0.04	$8.0^{+0.9}_{-0.5}$	0.11	0.48	0.25
SMACSJ2031−0768	$20^h31^m45\overset{s}{.}98$	$-40°37'31''$	>28.8	>28.4	26.38 ± 0.13	25.87 ± 0.11	$7.2^{+1.1}_{-1.3}$	0.30	0.25	0.02
SMACSJ2131−0444	$21^h31^m6\overset{s}{.}95$	$-40°18'57''$	>28.8	>28.4	24.38 ± 0.04	24.33 ± 0.06	$6.9^{+0.2}_{-0.1}$	0.98	0.00	0.00
SMACSJ2131−0516	$21^h31^m6\overset{s}{.}47$	$-40°18'51''$	>28.8	>28.4	25.07 ± 0.08	24.83 ± 0.09	$6.9^{+0.5}_{-0.2}$	0.78	0.16	0.00
SMACSJ2131−0567	$21^h31^m6\overset{s}{.}14$	$-40°18'23''$	27.61 ± 0.91	>28.4	25.24 ± 0.09	24.45 ± 0.06	$7.5^{+1.1}_{-0.4}$	0.35	0.46	0.11
Summed probabilities for objects with reliable photometry in all four bands:								11.6	5.6	1.6
Dropouts with defective F110W photometry[d]										
MACSJ0712−0414	$7^h12^m25\overset{s}{.}64$	$59°31'55''$	>28.8	>28.4	–	22.72 ± 0.02	$8.2^{+1.8}_{-0.4}$	0.21	0.31	0.31
MACSJ0712−0699	$7^h12^m29\overset{s}{.}23$	$59°32'59''$	>28.8	27.20 ± 1.55	–	23.69 ± 0.05	$6.5^{+2.0}_{-0.5}$	0.18	0.17	0.17
SMACSJ0549−0900	$5^h49^m16\overset{s}{.}25$	$-62°5'15''$	>28.8	>28.4	–	24.35 ± 0.05	$8.0^{+1.9}_{-0.9}$	0.23	0.24	0.24
SMACSJ0549−1009	$5^h49^m14\overset{s}{.}87$	$-62°5'46''$	>28.8	>28.4	–	23.68 ± 0.04	$7.9^{+2.0}_{-0.4}$	0.23	0.28	0.28
SMACSJ0549−9147	$5^h49^m11\overset{s}{.}29$	$-62°5'7''$	28.56 ± 2.22	>28.4	–	24.62 ± 0.07	$7.9^{+2.1}_{-0.9}$	0.22	0.23	0.23
Summed probabilities for candidates with defective F110W photometry:[e]								0.7	0.4	0.1
Net summed probability in each redshift bin:								12.2	5.9	1.7
Net detections reported in each redshift bin:								12^{+4}_{-3}	6^{+3}_{-2}	2^{+2}_{-1}

Notes. [a]68 per cent confidence intervals.
[b]P_7, P_8, and P_9 denote the probabilities that the object falls within redshift bins [6.5, 7.5), [7.5, 8.5), or [8.5, 9.5), respectively.
[c]Part of multiply lensed system; see Section 6.
[d]Reported probabilities for dropouts with defective *F110W* photometry are those derived directly from the BPZ fit, before application of a prior based on the redshifts of the other dropouts (see text).
[e]Summed probabilities reflect the prior described in the text and referenced in the immediately preceding note.

we eliminated from consideration; it was the large solid angle of the survey which permitted isolation of a significant number of more securely identified objects.

Spectroscopic investigations of some of our best candidates promise to better constrain these objects' redshifts, as do deeper space-based observations with more filters, and/or slitless near-infrared spectroscopy with WFC3 grisms. In addition, the eMACS Snaps programme proposes to survey 50 massive clusters with $z > 0.5$. Application of our method to this and other future programmes has the potential to isolate yet more promising candidates. Thus we confidently expect that the study of high-redshift galaxies will continue to shed light on the processes occurring in the early Universe.

ACKNOWLEDGEMENTS

We thank Anton Koekemoer for his invaluable advice concerning DRIZZLEPAC parameters, weight maps, and photometric errors. We also thank Hakim Atek for helpful advice regarding galaxy templates and extinction corrections. AR and HE gratefully acknowledge financial support from STScI grants GO-10491, GO-10875, GO-12166, and GO-12884.

REFERENCES

Atek H. et al., 2011, ApJ, 743, 121
Atek H. et al., 2014, ApJ, 786, 60

Atek H. et al., 2015, ApJ, 800, 18
Beckwith S. V. W. et al., 2006, AJ, 132, 1729
Benítez N., 2000, ApJ, 536, 571
Benítez N. et al., 2004, ApJS, 150, 1
Bertin E., Arnouts S., 1996, A&AS, 117, 393
Bolzonella M., Miralles J.-M., Pelló R., 2000, A&A, 363, 476
Boone F. et al., 2011, A&A, 534, A124
Bouwens R. J., Illingworth G. D., Blakeslee J. P., Franx M., 2006, ApJ, 653, 53
Bouwens R. J. et al., 2009, ApJ, 705, 936
Bouwens R. J. et al., 2010, ApJ, 709, L133
Bouwens R. J. et al., 2011, ApJ, 737, 90
Bouwens R. J. et al., 2012, ApJ, 752, L5
Bouwens R. J. et al., 2014, ApJ, 795, 126
Bowler R. A. A. et al., 2014, MNRAS, 440, 2810
Bradač M. et al., 2012, ApJ, 755, L7
Bradley L. D. et al., 2012, ApJ, 760, 108
Bradley L. D. et al., 2014, ApJ, 792, 76
Burgasser A. J., 2007a, ApJ, 658, 617
Burgasser A. J., 2007b, ApJ, 659, 655
Burgasser A. J., McElwain M. W., Kirkpatrick J. D., Cruz K. L., Tinney C. G., Reid I. N., 2004, AJ, 127, 2856
Burgasser A. J., Burrows A., Kirkpatrick J. D., 2006, ApJ, 639, 1095
Burgasser A. J., Liu M. C., Ireland M. J., Cruz K. L., Dupuy T. J., 2008, ApJ, 681, 579
Burgasser A. J., Cruz K. L., Cushing M., Gelino C. R., Looper D. L., Faherty J. K., Kirkpatrick J. D., Reid I. N., 2010, ApJ, 710, 1142
Calzetti D., Armus L., Bohlin R. C., Kinney A. L., Koornneef J., Storchi-Bergmann T., 2000, ApJ, 533, 682
Cardelli J. A., Clayton G. C., Mathis J. S., 1989, ApJ, 345, 245
Casertano S. et al., 2000, AJ, 120, 2747
Castellano M. et al., 2010, A&A, 511, A20
Chiu K., Fan X., Leggett S. K., Golimowski D. A., Zheng W., Geballe T. R., Schneider D. P., Brinkmann J., 2006, AJ, 131, 2722
Coe D., Benítez N., Sánchez S. F., Jee M., Bouwens R., Ford H., 2006, AJ, 132, 926
Coe D. et al., 2013, ApJ, 762, 32
Dey A., Graham J. R., Ivison R. J., Smail I., Wright G. S., Liu M. C., 1999, ApJ, 519, 610
Dressel L., 2014, Wide Field Camera 3 Instrument Handbook, Version 6.0. STScI, Baltimore
Ebeling H., Edge A. C., Henry J. P., 2001, ApJ, 553, 668
Ebeling H., Barrett E., Donovan D., Ma C.-J., Edge A. C., van Speybroeck L., 2007, ApJ, 661, L33
Ebeling H., Edge A. C., Mantz A., Barrett E., Henry J. P., Ma C. J., van Speybroeck L., 2010, MNRAS, 407, 83
Ebeling H. et al., 2013, MNRAS, 432, 62
Ellis R., Santos M. R., Kneib J.-P., Kuijken K., 2001, ApJ, 560, L119
Ellis R. S. et al., 2013, ApJ, 763, L7
Finkelstein S. L. et al., 2013, Nature, 502, 524
Giavalisco M. et al., 2004, ApJ, 600, L103
Güver T., Özel F., 2009, MNRAS, 400, 2050
Hildebrandt H. et al., 2010, A&A, 523, A31
Ishigaki M., Kawamata R., Ouchi M., Oguri M., Shimasaku K., Ono Y., 2015, ApJ, 799, 12
Jullo E., Kneib J.-P., 2009, MNRAS, 395, 1319
Kirkpatrick J. D. et al., 2010, ApJS, 190, 100
Limousin M. et al., 2015, preprint (arXiv:1510.08077)
Lorenzoni S., Bunker A. J., Wilkins S. M., Caruana J., Stanway E. R., Jarvis M. J., 2013, MNRAS, 429, 150
McLeod D. J., McLure R. J., Dunlop J. S., Robertson B. E., Ellis R. S., Targett T. A., 2015, MNRAS, 450, 3032
McLure R. J. et al., 2011, MNRAS, 418, 2074
McLure R. J. et al., 2013, MNRAS, 432, 2696
Madau P., 1995, ApJ, 441, 18
Magdis G. E., Elbaz D., Daddi E., Morrison G. E., Dickinson M., Rigopoulou D., Gobat R., Hwang H. S., 2010, ApJ, 714, 1740
Mann A. W., Ebeling H., 2012, MNRAS, 420, 2120
Mobasher B. et al., 2005, ApJ, 635, 832
Nakamura O., Fukugita M., Yasuda N., Loveday J., Brinkmann J., Schneider D. P., Shimasaku K., SubbaRao M., 2003, AJ, 125, 1682
Oesch P. A. et al., 2010, ApJ, 709, L16
Oesch P. A. et al., 2013, ApJ, 773, 75
Oesch P. A. et al., 2015, ApJ, 804, L30
Oke J. B., Gunn J. E., 1983, ApJ, 266, 713
Ono Y. et al., 2012, ApJ, 744, 83
Ouchi M. et al., 2004, ApJ, 611, 660
Pirzkal N. et al., 2015, ApJ, 804, 11
Postman M. et al., 2012, ApJS, 199, 25
Rafelski M. et al., 2015, AJ, 150, 31
Richard J., Pelló R., Schaerer D., Le Borgne J.-F., Kneib J.-P., 2006, A&A, 456, 861
Richard J., Stark D. P., Ellis R. S., George M. R., Egami E., Kneib J.-P., Smith G. P., 2008, ApJ, 685, 705
Richard J., Kneib J.-P., Limousin M., Edge A., Jullo E., 2010, MNRAS, 402, L44
Richard J., Kneib J.-P., Ebeling H., Stark D. P., Egami E., Fiedler A. K., 2011, MNRAS, 414, L31
Schaerer D. et al., 2007, A&A, 469, 47
Schenker M. A., Stark D. P., Ellis R. S., Robertson B. E., Dunlop J. S., McLure R. J., Kneib J.-P., Richard J., 2012, ApJ, 744, 179
Schenker M. A. et al., 2013, ApJ, 768, 196
Stark D. P., Ellis R. S., Bunker A., Bundy K., Targett T., Benson A., Lacy M., 2009, ApJ, 697, 1493
Steidel C. C., Pettini M., Hamilton D., 1995, AJ, 110, 2519
Steidel C. C., Giavalisco M., Dickinson M., Adelberger K. L., 1996, AJ, 112, 352
Steidel C. C., Adelberger K. L., Giavalisco M., Dickinson M., Pettini M., 1999, ApJ, 519, 1
Toft S., Gallazzi A., Zirm A., Wold M., Zibetti S., Grillo C., Man A., 2012, ApJ, 754, 3
Toft S. et al., 2014, ApJ, 782, 68
van Dokkum P. G. et al., 2014, ApJ, 791, 45
Vanzella E. et al., 2011, ApJ, 730, L35
Zheng W. et al., 2014, ApJ, 795, 93
Zitrin A. et al., 2013, ApJ, 762, L30
Zitrin A. et al., 2015, ApJ, 810, L12

This paper has been typeset from a TEX/LATEX file prepared by the author.